Sensitive absolute-gravity gradiometry using atom interferometry

J. M. McGuirk, G. T. Foster, J. B. Fixler, M. J. Snadden, and M. A. Kasevich
Physics Department, Yale University, New Haven, Connecticut 06520
(Received 25 May 2001; published 8 February 2002)

We report the demonstration of a sensitive absolute-gravity gradiometer based on light-pulse atom-interference techniques. The gradiometer consists of two absolute accelerometers operated in a differential mode. We report a differential acceleration sensitivity of $4\times10^{-9}g/\mathrm{Hz}^{1/2}$ and an inferred differential acceleration accuracy of less than $10^{-9}g$. This corresponds to a gravity-gradient sensitivity of $4E/\mathrm{Hz}^{1/2}$ ($1E=10^{-9}\,\mathrm{s}^{-2}$) and an accuracy of better than $1E$ for a 10-m separation between accelerometers. We demonstrate that the instrument can be used to detect nearby masses in a vibrationally noisy environment and characterize instrument sensitivity to spurious acceleration and rotation noise.

DOI: 10.1103/PhysRevA.65.033608 PACS number(s): 03.75.Dg, 39.20.+q, 04.80.−y, 32.80.Pj

I. INTRODUCTION

Precision gravimetry is scientifically and technologically relevant. For example, theories that predict violations of Einstein's general relativity are manifested in gravitational phenomenon such as composition-dependent gravitational forces, time variation of the gravitational constant G, or breakdown of the $1/r^2$ law [1]. Some theories predict a fifth force originating from a spin-gravity coupling [2]. The gravitational constant itself is only known to a few parts in 10^{-4} [3]. Technological applications lie in the fields of navigation, geodesy, underground structure detection, and oil and mineral exploration.

A technical problem associated with the characterization of gravitational forces is rooted in the equivalence principle: in principle, it is not possible to distinguish gravitationally induced accelerations from accelerations of the reference frame of measurement. In other words, gravimetry is fundamentally challenged by the inability to distinguish platform vibrations from gravitational accelerations. It is well known that this difficulty can be overcome with gradiometric measurements in which two simultaneous, spatially separated acceleration measurements are made with respect to a common reference platform. The difference between these acceleration measurements suppresses platform vibration noise as a common mode, but preserves gravitationally induced differential accelerations (gravity gradients). This nonlocal measurement of the curvature of the gravitational potential circumvents the equivalence principle and allows for characterization of gravitational anomalies in vibrationally noisy environments. For this reason gravity gradiometers are of technological interest.

In this paper we present a sensitive absolute-gravity gradiometer based on atom-interference methods. We demonstrate a differential acceleration sensitivity of $4\times10^{-9}g/\mathrm{Hz}^{1/2}$ (corresponding to an inferred performance of $2.8\times10^{-9}g/\mathrm{Hz}^{1/2}$ per accelerometer). We characterize instrument immunity to rotational and vibrational noise through laboratory shake tests. We measure the gravitational gradient induced by nearby mass distributions and characterize instrument accuracy. In previous work we made a proof-of-principle measurement of the gravitational gradient of the earth using a substantially less sensitive instrument [4].

The central idea behind our atom-interferometer gravity gradiometer is to make acceleration measurements on two vertically separated laser-cooled ensembles of cesium (Cs) atoms in free fall using a pair of vertically propagating laser beams: The propagation axes of these laser beams are aligned to pass through both ensembles. The light-pulse atom-interference method is used to measure the acceleration of each ensemble with respect to a reference frame defined by the phase fronts of the interrogating optical fields. The difference between the measured acceleration of each atom ensemble, divided by their separation, is a measure of the in-line component of the gravity-gradient tensor T_{ij}. (This tensor characterizes the gravitational-field inhomogeneity induced by nonuniform mass distributions.) Accelerations of the common reference frame—defined by the optical-field phase fronts—are rejected as a common mode in the difference.

Each acceleration measurement is accomplished by driving an optical pulse $\pi/2$-π-$\pi/2$ atom-interferometer sequence between the $6S_{1/2}$, $F=3$, and $F=4$ ground-state hyperfine levels of atomic Cs [5]. This method has recently been used by Chu and co-workers to measure g at the part-per-billion level, with a sensitivity of $2\times10^{-8}g/\mathrm{Hz}^{1/2}$ [6,7].

The interferometer theory is described in detail elsewhere [5,8]. Here we review the essential results. Each interferometer pulse couples two ground-state hyperfine levels via a two-photon, velocity-sensitive Raman coupling [9]. In the short, intense-pulse limit, the optical phase associated with the Raman coupling is imprinted on the atomic center-of-mass wave packets. This phase locates these wave packets with respect to the reference frame defined by the optical field. The following rules, derived from solutions of the Schrödinger equation for a two-level atom in the rotating-wave approximation, govern this imprinting process: $|3\rangle \rightarrow e^{i\phi(t)}|4\rangle$ and $|4\rangle\rightarrow e^{-i\phi(t)}|3\rangle$, where $\phi(t)$ is the phase of the driving field at the mean position $\mathbf{x}$ of the wave packet at the time t of the interferometer pulse, and states $|3\rangle$ and $|4\rangle$ are the two resonantly coupled hyperfine states. Explicitly, $\phi(t)=\mathbf{k}_{\mathrm{eff}}\cdot\mathbf{x}(t)+\phi_0(t)$. Here the Raman propagation vector $\mathbf{k}_{\mathrm{eff}}$ is defined as $\mathbf{k}_1-\mathbf{k}_2$; $\mathbf{k}_1$ and $\mathbf{k}_2$ are the wave vectors for two Raman lasers.

The probability following the three-pulse interferometer sequence for the atoms to be found in $|4\rangle$ (if they initially are

prepared in $|3\rangle$) can be evaluated from straightforward application of the above rules and is given by $P(|4\rangle)=[1-\cos\Delta\phi]/2$. The phase shift $\Delta\phi\equiv\phi(t_1)-2\phi(t_2)+\phi(t_3)$, where t_i is the time of the ith pulse. Evaluating $\phi(t_i)$ as in [5] gives $\Delta\phi=\mathbf{k}_{\rm eff}\cdot\mathbf{a}T^2+\Delta\phi_0$. T is the interrogation time between interferometer pulses, **a** is the mean acceleration experienced by the atoms with respect to the optical fields, and $\Delta\phi_0=\phi_0(t_1)-2\phi_0(t_2)+\phi_0(t_3)$. For vibrationally quiet environments, $\phi_0(t_1)=\phi_0(t_2)=\phi_0(t_3)$. In this case, $\Delta\phi_0=0$, and measurement of the transition probability following the three-pulse sequence determines **a**. In noisier environments, $\Delta\phi_0$ is no longer zero, and this spurious shift contaminates an individual acceleration measurement.

The gradient signal is derived from two simultaneous, spatially separated, acceleration measurements, which are made with respect to the same set of Raman-laser fields. This is accomplished by simultaneously measuring the fraction of atoms excited by the pulse sequence at both spatial locations. The differential acceleration is given by the differential phase shift, $\Delta\phi=\mathbf{k}_{\rm eff}\cdot\Delta\mathbf{g}T^2$, between the upper and lower atom ensembles, where $\Delta\mathbf{g}$ is the difference in the mean gravitational acceleration at the two accelerometers. In the framework of this analysis, low-frequency platform accelerations introduce common accelerations $\delta\mathbf{a}$, which cancel in the differencing procedure. High-frequency vibrational noise, which shows up in the $\Delta\phi_0$ terms of each accelerometer, also cancels.

Our approach differs from that used in other instruments. First, it uses atoms as proof masses rather than macroscopic objects. This eliminates variability from device to device and provides insensitivity to many environmental perturbations, e.g., temperature fluctuations and magnetic fields. The gradiometer references its calibration to the wavelength of the measurement laser, which is locked to an atomic spectral line, providing absolute accuracy and long-term stability. Because the sensitive axis is defined by the Raman propagation vector, and the acceleration measurements are referenced only to one retroreflector, the two accelerometers may be placed far apart without sacrificing common-mode vibration rejection. Increasing separation between accelerometers linearly increases the sensitivity to gravity gradients and provides insensitivity to near-field perturbations.

The gradiometer presented here performs favorably when compared with existing gravity-gradient sensors. The state-of-the-art mobile gradiometer is a device that uses mechanical mass-spring accelerometers on a rotating, gimballed fixture (Lockheed Martin UGM) [10]. This device has recently been used to perform airborne surveys of geophysical mass anomalies [11] and to characterize the gravitational anomalies from man-made underground structures [12]. Higher-sensitivity laboratory devices based on superconducting transducers have achieved significantly better sensitivities ($<0.1E/\mathrm{Hz}^{1/2}$) ($1E=10^{-4}\,\mathrm{s}^{-2}$) [13,14]. However, these devices suffer from tare effects in the superconductors [15] and their reliance on cryogens. More recently, the differential acceleration of two falling corner cubes has been measured using a Michelson interferometer configuration [16]. However, the demonstrated sensitivity of this device of $450E/\mathrm{Hz}^{1/2}$ is not competitive with the Lockheed Martin UGM, and it remains to be seen if this device can demonstrate the common-mode noise rejection required for mobile applications.

This remainder of this paper is organized as follows. Section II details the apparatus. Section III contains results characterizing the instrument's performance. Section IV draws comparisons with related atom-interference methods. Finally, future work is detailed in Sec. V.

II. APPARATUS

A. Apparatus overview

The apparatus is similar to that described in Ref. [4], but several changes have been made in order to achieve the current sensitivity. The apparatus consists of two laser-cooled and trapped sources of Cs atoms. The atoms are launched on ballistic trajectories and prepared in a particular internal state with optical and microwave techniques before undergoing the interferometer sequence. Following the interferometer sequence, atoms are detected using a normalizing detection method. Each of these stages is described below. In addition, we detail the operation of an actively controlled vibration-isolation system, which is used to validate our data-acquisition methodology.

B. Laser cooled atomic sources

Each laser-cooled atomic source consists of an ultrahigh vacuum system with a Cs source, which maintains a low Cs vapor pressure for a magneto-optical trap (MOT), along with the required laser beams and magnetic-field configuration to form the MOTs. The lasers are delivered to the vacuum chambers via optical fibers from a common high-power, frequency-stable laser system. The laser beams are configured in the six-beam [1,1,1] geometry (three mutually orthogonal pairs), which allows clear access for the Raman-interferometer beams along the the vertical axis.

In order to obtain good interferometer signal-to-noise ratios (SNRs), it is critical to load atoms quickly into the MOTs in a way that minimizes atom-number fluctuations during the loading process. A grating-stabilized diode laser (new focus vortex) replaces the previously used distributed-Bragg-reflector (DBR) laser as the master laser for the trapping system. The extended cavity of the vortex laser gives it an intrinsic linewidth approximately ten times smaller than the DBR laser. The vortex laser is locked to a Cs transition via standard saturation-spectroscopy techniques in a Cs cell. The locked laser has a stability of 1 $\mathrm{kHz/Hz}^{1/2}$ and an instantaneous linewidth of 300 kHz. The more stable master laser reduces the shot-to-shot rms number fluctuations of the MOTs by a factor of 5 to a SNR of 200:1. In addition, frequency-induced noise during the detection of the atoms following the interferometer is substantially suppressed with the use of this laser system.

The master laser injection locks two amplifier lasers, which then seed two 500-mW tapered amplifier lasers (SDL 8630E). All of the injection locks transfer the frequency stability of the master laser, without addition of extra frequency or intensity noise. Each tapered amplifier laser is split into

six equal outputs to provide the 12 trapping beams for the two MOTs. The splitting is accomplished using robust and compact free-space fiberoptic beam splitters (optics for research fiberbench). The stability of the fiber mounts maintains the splitting ratio to greater than 1% over many months with no adjustment. The fibers are polarization maintaining with an extinction ratio of greater than 30 dB. Polarization stability is further maintained with the use of clean-up polarizing optics at the output of the fibers (converting polarization drift in the fiber to negligible intensity fluctuations). The intensity and polarization stability of the MOT trapping beams contribute greatly to the reduction of the MOT number fluctuations. The trapping beams from the 12 fibers propagate uncollimated to the two MOTs. By not collimating the beams, we are able to circumvent window apertures limiting the beam size. Larger beam waists in the loading region lead to higher atom-loading rates. The approximate beam waist at the trapping position is 2.5 cm $(1/e^2)$, and the intensity is about $1.2I_{\mathrm{sat}}$ per beam ($I_{\mathrm{sat}}=1.1\ \mathrm{mW/cm^2}$ for the Cs cooling transition). In this configuration, each MOT loads approximately 2×10^8 atoms in 1 s.

After loading the MOTs from a thermal vapor for 1 s, the cold atoms are launched in ballistic, atomic-fountain trajectories. The launch is accomplished as follows. First, the detuning of the MOT beams is switched from -10 to -20 MHz from the cooling transition. Next, the trapping quadrupole magnetic fields are turned off, and the atoms are held in the -20-MHz detuned optical molasses for 30 ms while the eddy currents from the field switching damp out (the vacuum chambers are made of aluminum). For each MOT, following this holding period, the frequency of the upper three molasses beams is ramped down by 1 MHz over 5 ms [by applying the appropriate rf frequency shifts to an acousto-optic modulator (AOM)], while the frequency of the lower three beams is ramped up by an equal amount. This frequency ramp smoothly transfers the atoms to an optical molasses moving vertically at 1.5 m/s. After this ramp, the mean frequency of the trapping beams is ramped down to -40 MHz detuned (still in a moving molasses) over 5 ms, and then the intensity is ramped down to half intensity in 1 ms held for 0.5 ms, and ramped completely off in an additional 0.5 ms. These ramps cool the atoms to 2.3 μK (measured with stimulated Raman velocimetry). The frequency and intensity ramps are accomplished using digitally synthesized wave forms from Hewlett Packard HP8770A arbitrary wave-form generators (AWGs).

Following this launching and cooling phase, the cold atoms move in a 320-ms, 12-cm-high fountain during which they are prepared in a special state and then interrogated by the interferometer sequence.

C. State preparation

Before the atom-interference pulse sequence, a state-selection sequence prepares the atoms in the magnetically insensitive $m_f=0$ sublevel and velocity selects an atomic ensemble with a velocity spread, which is matched to the velocity selectivity of the Raman pulse sequence. This state selection, which is accomplished with a sequence of microwave and optical pulses, is important for obtaining high fringe contrast. The details associated with this state selection are discussed below.

Following their launch, atoms are initially distributed nearly evenly among the magnetic sublevels of the $F=4$ ground state. Three orthogonal pairs of magnetic-field coils, roughly in a Helmholtz configuration, zero the Earth's magnetic field and apply a vertical bias field of $\sim$100 mG. This bias allows selective addressing of individual $F=3$ to $F=4$ ground-state hyperfine transitions with a 9.2-GHz microwave field (delivered to the atoms through a Narda 640 X-band gain horn). First, a microwave composite π pulse transfers atoms from the $F=4$, $m_f=0$ to the $F=3$, $m_f=0$ sublevel. (Composite pulse sequences accomplish the population transfer associated with ideal π in an experimentally robust way, as described in the section below.) Next, a near-resonant pulse from the upper trapping beams tuned slightly above the $6S_{1/2}$, $F=4\rightarrow6P_{3/2}$, $F'=5$ transition clears atoms in the remaining $F=4$ sublevels (via the scattering force). Another composite microwave π pulse then returns $F=3$, $m_f=0$ atoms to $F=4$, $m_f=0$. An optical velocity-selective composite Raman π pulse is now applied, which transfers $F=4$, $m_f=0$ atoms within the velocity range encompassed by the Raman-pulse envelope to $F=3$, $m_f=0$. Finally, a second, near-resonant, blue detuned pulse clears away the remaining $F=4$ atoms. At this point, the remaining (state prepared) atoms are ready for use in the interferometer.

A considerable fraction of atoms are eliminated from the initial ensemble in this process: $\sim\frac{8}{9}$ from the internal state selection and another $\sim\frac{2}{3}$ in velocity selection, leaving roughly 4% for the interferometer.

1. Enhanced optical pumping

In order to increase the $m_f=0$ population, an enhanced optical-pumping scheme has been implemented. This method essentially recycles atoms that are not initially in the $m_f=0$ target state by a cyclic optical-pumping sequence. In practice we have seen as much as a factor of 3 improvement in usable atoms with this method.

The details of this scheme are as follows. First, a composite microwave π pulse is applied to drive atoms from the $F=4$, $m_f=0$ to the $F=3$, $m_f=0$ state as before. Then a depumping beam tuned to the $F=4$ to $F'=4$ transition is applied to optically pump the remaining atoms from $F=4$, $m_f\neq0$ to $F=3$ (where the prime still represents the $6P_{3/2}$ excited manifold). The depumping process redistributes the atomic population, with approximately $\frac{1}{7}$ of the remaining atoms ending up in $m_f=0$. The process is then reversed with a composite microwave π pulse transferring $F=3$, $m_f=0$ to $F=4$, $m_f=0$ followed by application of a repumping beam to the $F=3$ to $F'=4$ transition. In principle, this entire sequence could be repeated many times, resulting in 100% pumping efficiency.

In practice, inefficiency of the microwave pulses (described below), heating due to spontaneous emission in the pumping sequence, and the availability of only a finite amount of time to execute the sequence limit the process efficiency. We realize a factor of 3 improvement with just

one cycle of the sequence described in the previous paragraph.

For vapor-cell-loaded traps, the overall efficiency is also limited by the presence of the background atomic vapor. In this case, the depumping photons can excite atoms in the background vapor, which then emit light at the repumping frequency. These rescattered photons then redistribute atoms in the $F=3$, $m_f=0$ state to other $m_f \neq 0$ states. Thus there is a trade-off between background vapor pressure (which sets the loading rate) and the overall efficiency of the scheme (which works best at low vapor pressure). For our operating parameters, we typically realize a factor of 1.5–2 improvement.

Finally, we note that this method substantially increases shot-to-shot atom-number fluctuations (from 200:1 to 60:1). However, our normalized detection method is able to effectively suppress the impact of these fluctuations on the interferometer signals.

2. Composite pulse techniques

The above state-preparation methods work best with efficient coherent population transfer between $F=3$ and $F=4$ states. Less than unit transfer efficiency during a standard π pulse between the ground states can result from an inhomogeneous Rabi frequency of the microwave or optical pulse seen by the atoms, as well as by detunings due to the velocity spread of the atoms. In our apparatus, the microwave π pulses are typically only 80% efficient due to inhomogeneous field strengths across the atom clouds (since we drive the microwave transition with horns located outside the vacuum chamber). Furthermore, the state selection and optical pumping require a series of one optical and four microwave π pulses in the two separate chambers. With the current system, it is difficult to match the pulse conditions for all pairs of pulses due to different microwave intensity gradients in each chamber.

In composite pulse sequences [17], a standard π pulse is replaced with a sequence of pulses with variable area and relative phase. In our work, we employ a $\pi/2$-$\pi_{90°}$-$\pi/2$ pulse sequence in place of a π pulse. The subscript 90° indicates that the phase of the center π pulse is shifted 90° relative to the $\pi/2$ pulses. The use of this sequence increases the transfer efficiency of a pulse for inhomogeneous distributions of Rabi frequency and detuning across the atomic ensemble. Employing these pulses for the microwave state-preparation pulses increases the transfer efficiency from 80% with a regular π pulse to 95%. Figure 1 compares a frequency scan with regular and composite π pulses. More advanced interferometer pulse sequences may benefit from the use of composite pulses for the optical pulses but are not employed at the moment (see Sec. V A).

In comparison with the adiabatic rapid-passage (ARP) technique [18], composite pulses are easier to implement experimentally, and require less time (or total pulse area) to achieve efficient transfer. For example, we find that we need approximately 5π total time (here time is referenced to the time to drive a π pulse at the maximum Rabi frequency) for ARP to achieve results similar to those achieved with only 2π time for the composite sequence.

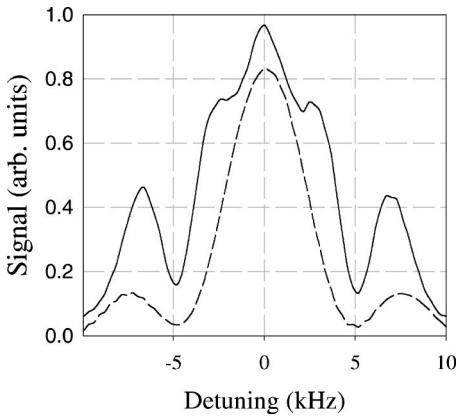

FIG. 1. A comparison of the transfer efficiency of a composite π pulse (solid traces) with a regular π pulse (dotted traces). The detuning is from the $F=4m_f=0 \rightarrow F=3m_f=0$ transition.

D. Atom interferometer

Following its launch and state preparation each atom ensemble is subject to the $\pi/2$-π-$\pi/2$ interferometer pulse sequence. Key experimental details associated with this sequence include the frequency stability of the lasers used to drive the Raman transition, optimization of the Raman excitation parameters, and the physical geometry for beam delivery.

1. Raman lasers

As the acceleration-induced phase shifts depend critically on the phase and wave vector associated with the laser beams used to drive stimulated Raman transitions, it is important to evaluate the possible contributions of laser-frequency noise to the relative stabilities of the interferometer signals. We first consider the constraints on laser-frequency stability, then describe the laser system we use to meet these constraints.

In our excitation geometry, the two ensembles are separated by ~1.4 m. The Raman fields propagate in an asymmetric way to these ensembles (see Fig. 2). To see this, con-

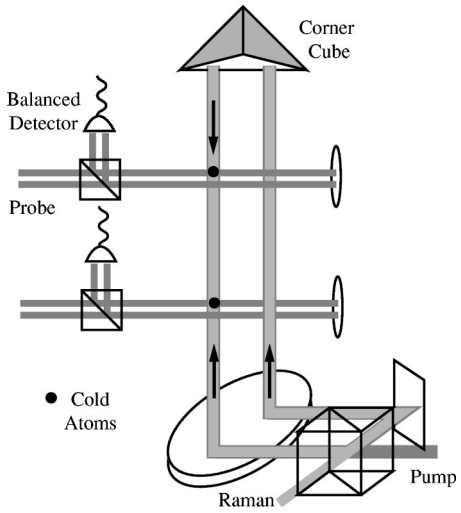

FIG. 2. Schematic illustration of the detection apparatus showing the Raman-beam race-track setup.

sider the propagation paths of the optical fields following the beam-dividing optic, which separates the two Raman fields. The beam of frequency ν_1 propagates roughly $x_1^1 \approx 0.3$ m before it passes through the first ensemble of atoms, while it propagates roughly $x_1^2 \approx 1.7$ m before it passes through the second ensemble. On the other hand, the beam of frequency ν_2 propagates $x_2^1 \approx 3.7$ m before it passes through the first ensemble, while it propagates $x_2^2 \approx 2.3$ m before it passes through the second ensemble.

If the frequency of the lasers drifts on a time scale short compared to the interrogation time T between pulses, this can cause an asymmetric phase shift to be read into the atomic coherences due to this path asymmetry. For example, suppose the laser frequency jitter is $\delta\nu$, while the differential path length traveled by the Raman lasers for the two ensembles is $\ell \equiv$ (effective path to ensemble 1) $-$ (effective path to ensemble 2) $= (x_2^1 - x_1^1) - (x_2^2 - x_1^2) \simeq 2.8$ m. This leads to a differential phase noise of $\delta\phi_{\text{laser}} \sim (k\ell)(\delta\nu/\nu)$. For a target interference SNR of 1000:1, $\delta\phi_{\text{laser}} \lesssim 1$ mrad. For our parameters, this implies $\delta\nu \lesssim 20$ kHz.

In order to achieve frequency stability at this level, a second vortex (external cavity, grating stabilized) laser is used as the master laser for the Raman-laser system. This laser is locked to the $6S_{1/2}$, $F=3 \rightarrow 6P_{3/2}$, $F'=2$ crossover resonance (via modulation transfer spectroscopy) using several AOMs to offset the frequency to obtain the desired detuning. The lock is maintained through the use of a digital signal processor (DSP, Spectrum Signal Indy TMS320C32). The DSP processes the lock error signal through a high-pass and low-pass channel, each operating at a sampling rate of 25 kHz. The high- and low-frequency channels provide feedback to the laser current and to the cavity piezoelement, respectively. Due to the presence of long-term drift in the piezoelement a third, very low frequency channel is provided through a GPIB command to the laser controller. The measured stability of the laser is comparable to that of the master laser used for the optical molasses (and is primarily limited by a 5-kHz resonance of the laser's piezoelectric transducer).

The vortex laser directly injection locks a 150-mW (SDD 5422) slave diode laser. This laser is then shifted up and down in frequency by 4.756 GHz (160 MHz above half the Cs clock frequency) with a high-frequency AOM. The diffracted orders are then used to injection lock two more 150-mW slave laser diodes at a frequency 700 MHz red detuned from the $F=3 \rightarrow F'=4$ and $F=4 \rightarrow F'=4$ transitions, respectively [19]. The frequency noise on the master Raman laser exists on both the slave lasers, but their frequency separation remains fixed at the Cs ground-state hyperfine transition. The detuning from the $F'=5$ level reduces the effect of spontaneous emission due to off-resonant single-photon excitations from each Raman beam.

2. Raman beam delivery

The Raman beams are delivered to the vacuum chambers with a polarization-maintaining optical fiber in order to increase the pointing stability of the Raman beams as well as to spatially filter them. Prior to coupling into the fiber, the two Raman beams are double passed through 80-MHz AOMs. These AOMs are controlled by another HP8770 AWG, which allows dynamic frequency, phase, and intensity tuning of the Raman beams during the interferometer pulse sequence. During the interferometer, the frequency of the Raman lasers must be chirped in order to maintain a resonance condition with the accelerating (Doppler shifting) atoms.

The two Raman beams are overlapped with orthogonal linear polarizations on a polarizing beam-splitting cube and passed through a Pockel's cell-polarization modulator (ConOptics 350-50) after the double-passed AOMs. The Pockel's cell is used to reverse the effective Raman-laser-propagation direction, as described below. The Raman beams then are coupled into a polarization maintaining fiber with 75% efficiency and sent to the gradiometer. For wave-front quality, after the fiber, the Raman beams are collimated with a 1.1 cm focal length aspheric lens in conjunction with a high-surface-quality 50-cm-focal-length spherical lens. This lens combination results in a uniform phase front for the Raman beams. After collimation the Raman beams have a 1.0 cm $(1/e)$ beam waist. All optics in the Raman beams' propagation path after the optical fiber are of high surface figure ($\lambda/10$ or better) in order to preserve the phase-front homogeneity of the Raman beams.

After collimation, the Raman beams enter a race-track geometry in order to obtain counterpropagating beams for the Raman interaction (see Fig. 2). The race-track configuration starts with a polarizing beam-splitter cube that separates the two orthogonally polarized Raman beams. The two Raman beams then parallel propagate vertically through the vacuum chambers with one beam passing through the axis of the atom ensembles and the other 2 cm off-axis. After passing through both chambers, a corner cube retroreflector redirects the off-axis Raman beam to counterpropagate with the on-axis Raman beam, resulting in two counterpropagating beams. The use of the corner cube decreases the tilt sensitivity of the apparatus by keeping the Raman-beam-propagation axis constant as the cube is subjected to spurious tilts. In this racetrack, standing waves are eliminated, which maintains overall intensity stability by suppressing etalon effects from the Raman beams. Also, spontaneous emission is reduced by half compared to using collinear retroreflected beams.

3. Raman propagation reversal

A technique to reduce many systematic interferometer phase shifts involves reversing the effective Raman propagation vector $\mathbf{k}_{\text{eff}} = \mathbf{k}_1 - \mathbf{k}_2$. Because the gravitational phase shift is proportional to $\mathbf{k}_{\text{eff}} \cdot \mathbf{g}$, reversing the sign of $\mathbf{k}_{\text{eff}}$ changes the sign of the gravitational phase shift. However, several systematic phase shifts, such as second-order Zeeman shifts from magnetic fields and any residual ac Stark shifts, have no dependence on the Raman wave-vector direction. Subtracting the phases obtained from consecutive experimental cycles using two reversed propagation directions gives twice the gravitational phase shift, but removes these systematic shifts. The propagation reversal is accomplished using Pockel's cell. The Pockel's cell rotates the polarization of both Raman beams by 90° when activated. This rotation causes the direction the Raman beams take through the race-

track to switch, i.e., $\mathbf{k}_{\text{eff}} \rightarrow -\mathbf{k}_{\text{eff}}$. Propagation direction can be switched from one shot to the next.

4. Raman beam parameters

A theoretical study of the interferometer contrast as a function of Raman-beam waist and detuning was performed. A finite Raman-beam size gives rise to a spatially inhomogeneous Rabi frequency across the atom cloud, causing dephasing during the interferometer. Similarly, the velocity spread of the atoms along the Raman beams causes inhomogeneous broadening due to differential Doppler shifts across the atom ensemble. Typical Rabi frequencies are around 30 kHz, and the initial width of the thermal spread of the atom ensemble is about 45 kHz. Incorporating the finite beam size and the initial atomic-velocity distribution function into our analysis, we find an optimal 35% contrast for a Raman-beam waist of 1.0 cm radius $(1/e)$, and a detuning of ≈ 1 GHz from $F'=5$ (our chosen operating point).

In addition to the interferometer contrast, systematic ac Stark shifts were studied. ac Stark shifts from the Raman pulses themselves cause spurious phase shifts in the interferometer if unconstrained. However, with a two-photon Raman transition, the ac Stark shift is the difference between the individual ac Stark shifts from each beam and can be zeroed by adjusting the ratio between the two Raman beams. The Stark shift is balanced with a beam-intensity ratio of $\sim 1.6{:}1$ for the chosen Raman detuning. The Stark shift is balanced empirically by inserting off-resonant Raman pulses within a microwave $\pi/2$-π-$\pi/2$ interferometer and adjusting the Raman-beam-intensity balance to the zero of the optically induced phase shift. This ratio of 1.6:1 for the chosen Raman detuning agrees well with theoretical predictions.

5. Interferometer operation

The gradiometer is typically operated in its most sensitive configuration with the interferometer pulses at a maximal spacing of $T=157.5$ ms. This time is limited by the vacuum-chamber size, which constrains the fountain height to 12 cm. Following the three-pulse interferometer sequence, the population distribution of the atoms in each ensemble is measured. In order to extract the gravitationally induced phase shift, the phase of the final interferometer pulse needs to be scanned. The scanning is accomplished digitally with the AWG by scanning the phase of the rf wave form applied to the low-frequency AOMs in the Raman-beam paths. This phase scanning is in addition to the frequency chirp applied during the pulse. The total cycle time is 0.7–1.4 s, depending on the trap-loading parameters.

E. Detection system

1. Detection apparatus

In order to realize high interferometer sensitivity, atoms must be detected with a high SNR following the interferometer pulse sequence. Our detection system uses a balanced, modulation-transfer technique to reduce laser-induced detection noise and differentiate cold atoms from thermal-background atoms. This detection method is described in [20] and is summarized here.

Balanced detection uses two parallel, horizontally propagating probe beams, separated vertically by 2.5 cm, to detect atoms in one or both states following the interferometer. The absorption of the probe beams by the atoms is detected on a balanced photodiode with two inputs that are subtracted before amplification. Typically, the absorption by the cold atoms is around 0.1%.

We use two detection pulses as follows. Following the interferometer, atoms in the $F=4$ state are detected by pulsing on near-resonant probe beams for 4.6 ms when the atom cloud is in the upper detection beam. During this pulse, the mean velocity of the $F=4$ atoms is slowed to rest by optical forces induced by the detection beams. Atoms in the $F=3$ state continue to fall, however. When these atoms intersect the lower probe region, atoms in the $F=4$ state have not moved out of the upper detection region. Pulsing on the probe beams for another 4.6 ms following a short repumper pulse measures the differential absorption between the two hyperfine states. These two pulses provide sufficient information to infer the overall transition probability in a way that is immune to shot-to-shot fluctuations in the total atom number. We have shown that this method is immune to laser frequency and amplitude technical noise as well [20].

In addition, a modulation-transfer technique is employed to remove noise from the thermal-background vapor. Here a frequency-modulated (FM) pump beam is applied along a vertical axis orthogonally to the probe beams during each detection pulse. The nonlinear interaction between the FM pump and the atoms modulates the complex index of refraction of the atoms. This modulation produces an amplitude modulation (AM) on the probe beams [21,22]. The AM is detected by the balanced detector, mixed down to dc with a double-balanced mixer, and integrated with a Hewlett Packard 3458A multimeter. The orthogonality of the pump and probe beams provides a velocity selectivity that allows rejection of signals from the fast-moving thermal-background atoms.

2. Detection noise analysis

The amplitude of the modulated absorption signal at the photodiode is about 0.8 pW per atom. The detection photodiodes have noise-equivalent powers corresponding to a 60-atom detection sensitivity in the 4.6-ms measurement window. The digital voltmeters that acquire the signal from the photodiodes are only slightly noisier with a noise floor corresponding to 100 atoms. The largest contribution to the intrinsic noise comes from the detection light itself. Because absorption detection is used and the absorption is small, there is a substantial amount of unabsorbed light, greater than 99%, striking the detector. Shot noise on the number of photons incident on the detector during the integration window is the leading intrinsic noise source. The shot-noise power is 0.25 nW, resulting in a minimum detectable signal of ~ 300 atoms. This noise dominates the technical noise sources.

There is also a noise component of similar size due to a small number of atoms in undesired states that survive the state preparation. Slight changes in laser frequency and selection pulse efficiency during the state preparation cause

this number to fluctuate. However, this noise source is common between the two chambers and is also suppressed by the balanced-detection method.

To summarize, the noise of our detection system allows detection of transition probability at the atom shot-noise limit when we detect more than $\sim 10^5$ atoms. These noise limits are discussed in the context of our overall instrument sensitivity below.

F. Signal extraction

1. Interference fringe fitting

As described above, the phase of the final interferometer pulse is scanned electronically. A straightforward method of extracting gravity-gradient information is to determine the gravitationally induced phase shifts in each atom ensemble by performing least-squares sinusoidal fits on the observed interference fringes. This is possible when vibration-induced phase noise is $\lesssim 1$ rad. The gravity gradient is obtained by subtracting the two phase shifts from each other. Vibrational phase noise and local oscillator phase noise cause the phase extracted by the sine fits to be shifted. However, these noise sources couple to the two accelerometers in a common-mode way. This common-mode behavior results in the two sinusoidal fits being shifted by an identical amount, and any effect of common-mode noise is cancelled in the subtraction used to obtain the gravity gradient. We study the statistics of the resulting phase differences under static gravity-gradient conditions to estimate instrument noise.

We find that the distribution of the residual noise contains outlying points. Eliminating these outlying points increases the SNR by up to a factor of 6. The reduction of the number of points is incorporated into the data-collection time in determining the sensitivity. We are presently studying possible sources of this noise component.

The ratio of the interference-fringe amplitude to the standard deviation of the phase-difference distributions determines the instrument SNR. The side of a fringe, i.e., the linear slope of a sine wave, is most sensitive to phase shifts with a sensitivity given by $\delta\phi = 1/_{\mathrm{SNR}}$. For gravitationally induced phase shifts, the sensitivity to a change in the gravitational acceleration is $\delta g = \delta\phi/(2kT^2)t^{1/2}$, where t is the data-acquisition time to achieve the uncertainty $\delta\phi$. Dividing by the chamber separation determines the sensitivity to gradients.

2. Magnetic phase shifting

Good common-mode noise suppression requires that the lower and upper chamber fringes be acquired in phase. However, the earth's gravity gradient of $\sim 3000E$ will cause a relative phase shift of ~ 1.5 rad between the two chambers. In order to accommodate this shift, a bias magnetic field is pulsed on for 67 ms in the lower chamber during the atom interferometer. This field pulse causes a phase shift due to the second-order Zeeman effect. The amplitude of this pulse is chosen to produce a shift that compensates the shift due to the gravity gradient, allowing both fringes to be acquired in phase.

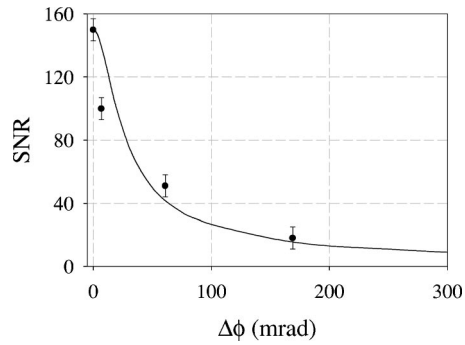

FIG. 3. The decrease in the gradiometer SNR is shown due to a phase mismatch induced by the Earth's gravity gradient. The phase shift $\Delta\phi$ is the gradient phase shift from increasing the interferometer time T ($\Delta\phi \propto T^2$). The solid line is a theory based on the noise from two mismatched sine waves in quadrature with photon shot noise from the detection system.

We have quantitatively studied the effectiveness of common-mode noise suppression as a function of the phase alignment of the interferometer fringes. Figure 3 shows a comparison of the predicted dependence of the noise on the relative phase between fringes with experimental SNR data. For simplicity, we scanned the relative phase between pulses simply by changing the interrogation time T. (For this study, we disabled the magnetic phase shifter and worked with relatively short interrogation times.) The data shown in Fig. 3 is the SNR of the phase difference between the two fringes obtained by performing least-squares fits as described above on a set of interference fringes. The prediction is the simulated SNR of the phase difference between two phase-mismatched sine functions with phase noise added. The predicted SNR is added in quadrature with uncorrelated detection noise in order to compare the simulation with experimental data in this curve. As shown, the data is in good agreement with the theory, demonstrating the need for the magnetic phase-shifting pulse.

The stability of the bias field used in the magnetic shifter has also been studied. Noise on this bias field could lead to extra phase noise in the gravity-gradient signals. This noise has been investigated by applying a bias pulse in a microwave clock $\pi/2$-$\pi/2$ experiment and comparing the SNR for a weak pulse (phase shift ~ 1.2 rad) and a strong field pulse (phase shift ~ 67 rad). For the large phase shift, no extra phase noise or drift is seen at a fractional uncertainty in the phase of less than 3×10^{-6}. This implies that for a 1-rad shift, the bias pulse contributes noise at a level below $8\times 10^{-13} g$.

3. High phase noise regimes

In the case where phase noise is greater than 1 rad, the noise renders it impossible to characterize instrument noise using the least-squares method described above. In the most sensitive modes of operation, the vibrations of the reference platform induce phase noise much larger than this level. A different analysis technique must be performed in this regime, using a point-by-point analysis. After collection of the gradiometer data, a signal extraction algorithm removes am-

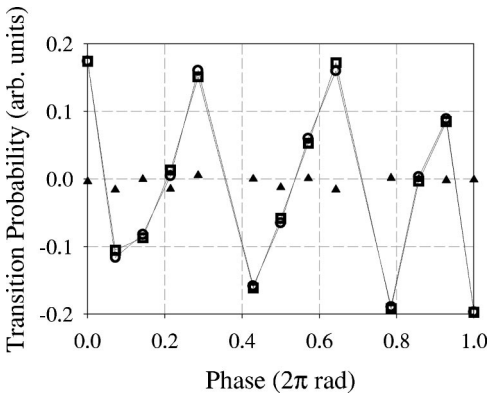

FIG. 4. Gradiometer interference fringes with $T=157.5$ ms. Squares and circles represent the normalized upper- and lower-chamber fringes, respectively, after compensating for contrast differences between the chambers. Triangles show the lower-chamber signal residuals.

plitude and phase noise from the signals: Our detection method allows measurement of the number of atoms in the $F=4$ state and the population difference between the two states. With this information, common amplitude fluctuations in each chamber, primarily from number fluctuations from the MOT loading, can be removed. After removing amplitude noise; a cross-chamber normalization is performed to reject phase noise that is primarily vibration induced.

The details of this noise-analysis procedure are as follows. After each interferometer cycle (which represents one gradient measurement) two samples are acquired in each accelerometer: signals proportional to the $F=4$ population and to the differential population (i.e., proportional to the number of atoms in $F=4$ minus the number of atoms in $F=3$). The two samples are combined to infer the total number of atoms present in the interferometer during each experimental cycle. The $F=4$ signal is then divided by this total atom number to remove any fluctuations in the amplitude of the $F=4$ signal from shot-to-shot atom-number fluctuations. We normalize each interferometer with this procedure. To remove common phase noise between the two chambers, a series of experimental cycles is taken, and a least-squares minimization (*via* Gaussian elimination) is performed on the quantity $(S_1-\alpha S_2-\beta)^2$ where S_1 and S_2 are the shot-by-shot normalized $F=4$ population levels from the two interferometers. The fit constants α and β are used to compensate for possible differences in interference contrast between the two accelerometers.

The residuals of the Gaussian-elimination procedure are used to estimate instrument noise, as shown in Fig. 4. Again, this distribution is non-Gaussian, and outlying points are discarded to obtain SNR and short-term sensitivity estimates.

Note that while this method is suitable for characterization of the instrument noise floor under static-gradient conditions, further work is need to demonstrate effective algorithms for extraction of dynamic gradient signals (such as would be present in moving-platform applications). We are currently exploring algorithms for this purpose.

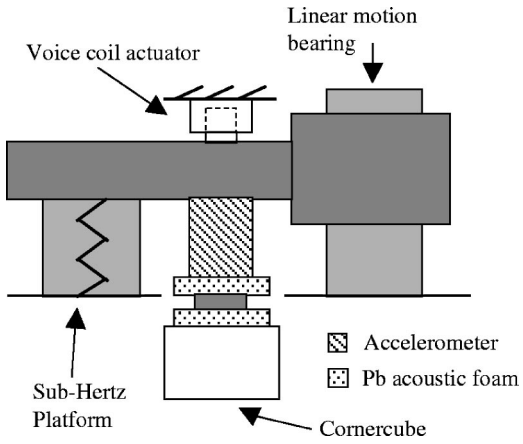

FIG. 5. Schematic of the vibration-isolation apparatus featuring elements for passive and active isolation.

G. Vibration-isolation subsystem

At the most sensitive gradiometer operation, vibration phase noise is large, and the high phase-noise algorithm is employed. However, in order to verify the validity of this algorithm, a vibration-isolation system was constructed to remove most of the vibration-induced phase noise from the interference fringes. With this reduction in phase noise, the least-squares fit algorithms also can be used to reduce the data.

1. Mechanical design

The primary object in the instrument that must be isolated from vibrations is the Raman-beam corner cube. All other optics are positioned so that any vibrations Doppler shift the two Raman beams in a common way, and the Raman difference frequency remains unchanged. The Raman-beam corner-cube retroreflector is mounted on a Newport sub-Hertz platform (SHP), which provides the principal vibration isolation (see Fig. 5). The SHP is guided by a linear air bearing (New Way S4010002) along the vertical axis. The SHP provides isolation in the range of 0.5–40 Hz. An accelerometer (Teledyne Geotech S-510) is mounted on the SHP to monitor platform accelerations. The corner cube is attached to the platform by a stack of two pieces of 1-in-thick lead-filled acoustic foam separated by a 0.5-in-thick sheet of aluminum. The double stack of acoustic foam reduces vibrations of 30 Hz and higher by more than 20 dB. A linear voice-coil actuator provides active feedback to the SHP. Additionally, the voice coil can be used to drive platform accelerations; this shake testing is the subject of Sec. III B.

2. DSP servo system

Here we describe the active servo system for the SHP platform. The active feedback loop starts with the accelerometer to monitor vibrations. The accelerometer output is processed by a DSP (Spectrum Signal Indy TMSB20C32), which we use to filter digitally the accelerometer input (as described below) and generate the feedback error signal. The feedback signal, after being buffered by a voltage amplifier, closes the feedback loop by driving the voice coil mounted

between the SHP and the platform support. We apply the following digital filters in processing the accelerometer signal. First, a lag filter with a bandwidth of 1–80 Hz rolls off the feedback below the accelerometer's 100 Hz high-frequency cutoff. Next, a second lag filter with identical bandwidth is used to make the gain roll-off second order. Finally, two lead filters are applied to keep the system from oscillating at low frequency near the closed-loop SHP resonance of 0.03 Hz, which is also close to the internal high-pass frequency of the accelerometer. The two lead filters have bandwidths of 38 mHz–200 Hz and 380 mHz–200 Hz, respectively. The total gain of all four filters is 1600. This work is similar in concept to that reported in Ref. [23].

Using this servo, we are able to reduce the vibrations to near the noise floor of the accelerometer ($10^{-8}g/\mathrm{Hz}^{1/2}$) over a bandwidth of 40 mHz–25 Hz. Higher frequencies are passively attenuated by the acoustic foam. With the addition of the vibration-isolation system, phase noise from accelerations of the corner cube is reduced to less than 1 rad, and least-squares sinusoidal fits may be performed on the fringes for the longest interrogation times.

H. Microwave generation

The generation and delivery of the 9.2-GHz microwave field is briefly described here. The microwave field is coupled to the atoms through rf horns attached to view ports on the MOT chambers. The microwave frequency is tied to a 10-MHz reference, temperature-stabilized, master crystal oscillator (Oscilloquartz OCXO, stability of 1.4×10^{-13} in 1 s). The reference oscillator drives a 100-MHz phase-locked oscillator (PLO, Wenzel 500-0732), which is the input to a Microlambda (MLPE 1162) 9.2-GHz PLO. The rf is mixed in a single-sideband mixer with an ~7.4-MHz signal from an AWG, which is also phase locked to the reference oscillator. The AWG is used to scan the rf frequency and phase. The mixer output is amplified up to ~1 W and sent to the horns. The rf power is controlled by the AWG output, and the relative power to the two chambers can be adjusted with appropriate attenuation in the two paths.

We perform a microwave $\pi/2$-$\pi/2$ clock experiment as a diagnostic to check the phase-noise performance of our oscillators and the noise performance of our detection system. We have shown that we can detect microwave-clock fringes with 1000:1 SNR using our normalized detection [20]. This SNR is at the atom shot-noise limit for our fountain with no velocity selection (~10^6 atoms/shot).

III. INSTRUMENT PERFORMANCE

A. Sensitivity

Each interference fringe is typically recorded with 15 consecutive cycles of the experiment. The number of points per scan is kept small to decrease sensitivity to long-term drifts in signal amplitude and contrast. The source of such drifts include fluctuations in laser power and drifts in the Cs vapor pressure in the vacuum chambers. The normalized data-reduction method described in Sec. II F is performed on the data. The resulting observed SNR is typically 150:1. This

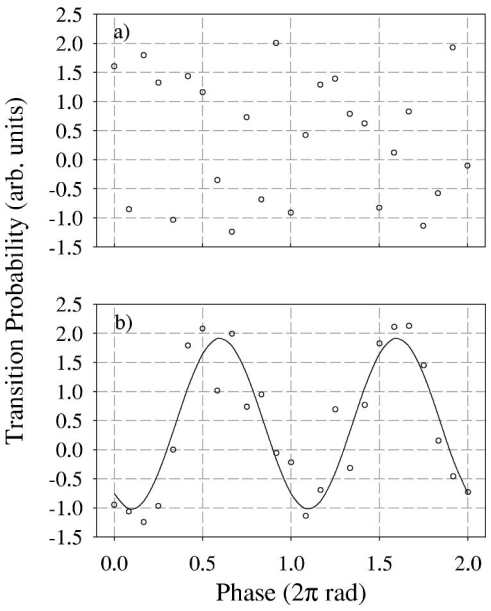

FIG. 6. Gradiometer interference fringes with $T=157.5$ ms. Circles represent the raw data points and the solid line is a sinusoidal least-squares fit. (a) shows a fringe with the inertial reference platform, i.e., the corner cube, rigidly attached to the optical table. (b) shows an interference fringe taken with the corner cube mounted on the vibration control system.

corresponds to a differential accelerometer performance of $4\times10^{-8}\ \mathrm{m/s^2/Hz^{1/2}}$, or ~$4\times10^{-9}g/\mathrm{Hz}^{1/2}$. Scaling this to a 10-m baseline gives an inferred gradient sensitivity of $4E/\mathrm{Hz}^{1/2}$. Figure 4 shows typical high-sensitivity fringes in the upper and lower chamber for a $T=157.5$ ms interferometer. The fringe contrast is typically ≈33%.

Figure 6 compares interference phase scans with the reference platform rigidly attached to the optical table (~$10^{-5}g$ technical acceleration noise) with the reference platform servoed using the vibration-isolation system. We can use the data acquired under servoed conditions [e.g., Fig. 6(b)] to provide an independent check on the observed SNR, by performing the least-squares-fitting analysis detailed in Sec. II F 1, and comparing it with the point-by-point analysis of Sec. II F 3 for data acquired without the servo [e.g., Fig. 6(a)]. We find that both approaches yield consistent noise estimates.

1. Noise

The dominant noise source is atom shot noise: the Poissonian fluctuations that arise from detecting atoms in coherent superposition states, also called quantum projection noise [24]. Atom shot-noise scales as the square root of the number of atoms detected. As long as there is a sufficiently large number of atoms contributing to the interference fringes, this noise source will be the dominant noise source.

For the $T=157.5$ ms gradiometer, the demonstrated SNR is predominantly limited by atom-number shot noise. The fringe amplitude corresponds to about 2.5×10^5 atoms. At 33% fringe contrast, there is a mean offset of 7×10^5 atoms. Based on atom shot noise, these atom numbers put a limit of 300:1 on the SNR for each interference fringe

$[2.5\times10^5/(7\times10^5)^{1/2}]$. Additionally, normalizing each chamber reduces the SNR for each gravimeter to $(300/2^{1/2}):1$. Subtracting the two gravimeter signals to produce a gradient signal decreases the SNR by another factor of $2^{1/2}$, fundamentally limiting the SNR for the full-gravity gradiometer to 150:1.

The noise produced from photon shot noise on the unabsorbed portion of the probe detection light, corresponding to ~300 atom minimum detectable signal, is approximately at the 800:1 level for each individual fringe, giving about a 400:1 limit after the normalization and subtraction of the two fringes. This means that photon shot noise does not impose a substantial SNR limit for the current number of atoms, but it would become significant for reduced atom numbers.

2. Mass detection

In order to demonstrate further the sensitivity of the gravity gradiometer, measurement of the gradient of a nearby object was performed. Previously, the Earth's gravitational gradient was measured [4]. With the improved sensitivity, a measurement of the gravity gradient from small test masses has been made. For this measurement, eight lead bricks (~12.5 kg each) were stacked symmetrically about the lower chamber, ~0.2 m from the apex of the atomic fountain. The calculated acceleration from this configuration of mass should yield a $8.2\times10^{-9}g$ signal. The measured acceleration is $(8.1\pm2.1)\times10^{-9}g$, which agrees well with the expected phase shift.

We are currently extending this work to measure the gradient of a well-characterized mass. Our goal is to measure G, the gravitational constant, at the part-per-thousand level.

B. Immunity to environmental noise

An important feature of the gradiometer is the ability to reject common-mode accelerations in the two measurements. This is critical for a device, which might used on a moving platform. In order to demonstrate this capability, we performed a series of acceleration and tilt tests to characterize the instrument's sensitivity to platform vibration and tilt noise. We characterize the effects of accelerations and tilts by measuring instrument SNR as a function of the amplitude and frequency of an external platform drive.

1. Linear acceleration

We characterized immunity to linear accelerations by shaking the platform on which the retroreflecting corner cube is mounted. As in earlier work, this corner cube plays the role of the acceleration reference for the acceleration measurements [8,4]. We drive the platform by applying sinusoidal drive currents to the voice coil coupled to the vibration-isolation platform. We monitor the resulting platform acceleration with the platform accelerometer (described in Sec. II G U). For this work, the high-frequency lead-foam passive isolation between the platform and the corner cube was removed. This study was done with the interferometer operating in its most sensitive configuration (at $T=157.5$ ms interrogation time). Figure 7 summarizes the results of these tests. For frequencies in the range 1–100 Hz no

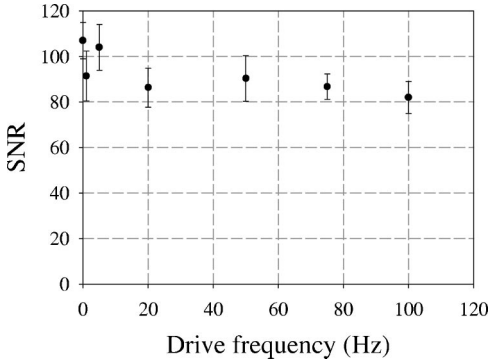

FIG. 7. Results of the reference-platform shake test. No SNR reduction is seen when driving accelerations on the reference platform at amplitudes of $10^{-2}g$ over the frequency band indicated. This amounts to 140 dB of vibration rejection. The observed maximum SNR is slightly reduced from the data of Fig. 5

significant degradation of the SNR was observed for drive amplitudes up to $2.5\times10^{-2}g$. This corresponds to a common-mode rejection ratio of 140 dB. At amplitudes greater than ~0.1 g, the accelerations are large enough that individual Raman pulses are Doppler shifted out of the Raman resonance condition. At this point, we observe poor interference fringe contrast.

2. Rotation

Tilts of the Raman interferometer beams are expected to degrade the sensitivity of the measurement. In order to study the effects of small tilt displacements, we floated the optical table on which the gradiometer apparatus was mounted using commercial pneumatic legs (Newport I-2000). We drove tilt motions with an appropriately placed voice coil and characterized these motions using a tilt meter (Applied Geomechanics 755-1129; specified resolution of 1 μrad, 20 Hz bandwidth). The rotation vector associated with the tilt motion was in a plane perpendicular to the Raman-propagation axis. Figure 8 shows observed SNR versus maximum tilt amplitude for different driving frequencies.

Both centrifugal and Coriolis forces lead to a degradation in instrument sensitivity. A rotation Ω generates a centrifugal

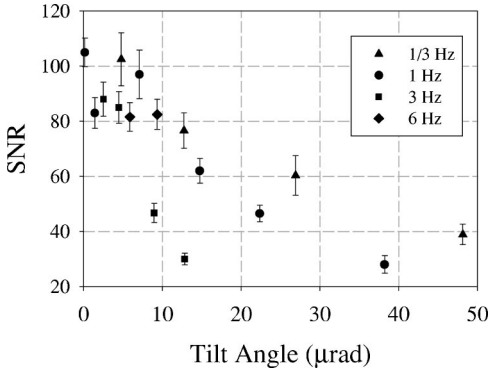

FIG. 8. Results of the platform-tilt test. The floated optical table is tilted at a number of frequencies, and the gradiometer is insensitive to a range of tilt amplitudes. The observed maximum SNR is slightly reduced from the data of Fig. 5

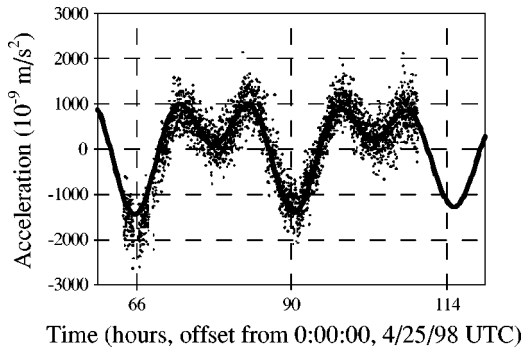

FIG. 9. Gravitational tidal signals as monitored by one accelerometer output over two days. Data are scattered points and the solid line is the tidal model with no free scaling parameters.

acceleration $R\Omega^2$, where R is the distance of one accelerometer from the center of rotation. For two accelerometers separated by distance δR, the differential acceleration is $\delta R\Omega^2$, while the acceleration gradient is Ω^2. For our operating parameters, we expect this mechanism to begin to degrade the SNR at $\Omega \sim 10^{-4}$ rad/s. However, full loss in SNR is not expected until $\Omega \sim 10^{-3}$ rad/s for this mechanism, much higher than the rotation rates employed in this study. The Coriolis force leads to a loss in fringe contrast. In this case, the source transverse velocity spread of $\delta v \sim 3$ cm/s leads to an interference phase spread of $\delta\phi \sim 2k_{\rm eff}\delta v\Omega T^2$. At $\Omega \sim 10^{-4}$, $\delta\phi \sim 1$ rad, and we expect a full loss in contrast. This is in reasonable agreement with our observations.

C. Accuracy estimation

To demonstrate accelerometer (hence gradiometer) accuracy, we monitored accelerometer outputs over extended periods of time. As in [6] we observed the daily fluctuations in the measured acceleration due to gravity induced by the motion of the sun and moon. Figure 9 shows data from one accelerometer taken over a period of several days compared to the Tamura 87 tide model [25]. The only free parameter in this fit is an overall phase offset. From this data set, we constrain the accelerometer phase offset to better than $10^{-9}g$ over the two-day measurement cycle. Subsequent measurements, taken several weeks later, resulted in a similar determination of the fitted offset. From these measurements we infer an accelerometer accuracy of $<10^{-9}g$ over time periods of days. For a 10-m baseline gradient instrument, this corresponds to an inferred accuracy of better than $1E$. Further accuracy studies are underway.

IV. DISCUSSION

In this section we discuss the light-pulse method in the context of other de Broglie wave-interference methods based on laser-atom interactions, as well as alternate geometries for gradient measurements.

A. Interferometer comparisons

Here we compare de Broglie-wave gravimeters based on multiple-pulse techniques using stimulated Raman transitions, Bragg scattering, diffraction in the Raman-Nath regime, adiabatic transfer, and the ac Josephson effect with Bose-Einstein condensates (BEC).

We have recently demonstrated large-area, multiple-Raman-pulse techniques that may enable higher sensitivity gravimeters and gradiometers [26]. By using extra stimulated Raman-transition pulses of alternating propagation direction, a large relative momentum can be transferred to the two interfering atomic wave packets, resulting in a large-area interferometer. The sensitivity of this device to gravitational phase shifts increases linearly with the relative momentum imparted to the wave packets, or the number of extra pulses applied. For instance, a gradiometer with one extra set of pulses has a relative splitting of $6\hbar k$ and a sensitivity to gravity gradients given by $\Delta\phi = 6\mathbf{k}\cdot\Delta\mathbf{g}T^2$. In principle, each subsequent Raman pulse should not affect the fringe contrast, except for a small amount of spontaneous emission. This process should be extendable to a large number of extra pulses and a large relative momentum.

This method might be extended using special sequences of composite pulses (see Sec. II C 2). The benefits of using composite pulses in this context would be an extremely large input-velocity acceptance for a fixed Rabi frequency and robust suppression of spatial inhomogeneities in Rabi frequency (which arise due to the finite size of the Raman laser beams). For example, consider the following sequence. A high-efficiency composite microwave pulse could be used for the initial $\pi/2$ pulse. Next a composite optical π pulse gives the wave packets $4\hbar k$ momentum splitting, and after a long drift time two composite π pulses redirect the wave packets back towards each other. Finally, a last composite optical pulse and another composite microwave pulse recombine the wave packets to complete the interferometer. Simulations show that this larger-area interferometer has the potential to have a very high fringe contrast (because of the symmetric composite pulses).

Bragg-scattering-based interferometers diffract atoms from standing waves of laser light. As in the light-pulse interferometers, these interactions can be configured as atom-optic beam splitters and mirrors [27]. The primary virtue of Bragg-scattering interferometers is that the atoms always remain in the same internal state. This reduces the sensitivity to systematic phase shifts such as Zeeman shifts and ac Stark shifts, since the wave packets in each arm of the interferometer experience symmetric phase shifts due to these effects. In comparison, the Raman method requires the use of propagation-vector-reversal techniques to gain immunity to these possible systematics. Furthermore, high-order Bragg processes can be used to create large-area, high-sensitivity instruments. However, high-order Bragg processes operate efficiently over a relatively narrow range of initial atomic velocities (significantly less than a photon recoil velocity). This severely constrains the fraction of atoms that can contribute to the interference signal, and thus the atom counting rate. On the other hand, BEC or atom laser sources may eventually produce extremely bright atomic beams (having excellent velocity collimation). In this case, Bragg processes may become a competitive choice for interferometer sensors.

A gravimeter based on diffraction in the Raman-Nath regime has been demonstrated [28]. In this interferometer, short, intense pulses of light are applied to the atomic ensemble. Due to the shortness and intensity of these pulses, atoms are diffracted into a large number of diffraction orders. Two such Raman-Nath pulses are used to construct the interferometer, and because of the widespread of wave packet momenta, many different interfering paths exist. Some of these paths overlap and interfere after an echo time, and the echo time determines the sensitivity to gravitational phase shifts. The Raman-Nath diffraction also populates many higher-lying momentum states that do not contribute to the closed interferometer paths, which decreases the interferometer contrast and places severe constraints on the SNR. High-sensitivity gravimeters, which require good SNR for their operation, have yet to be demonstrated using this approach [29].

Adiabatic transfer recently has been used in a proof-of-principle demonstration of a possible large-area interferometer [30]. In this approach, atoms are put into coherent superpositions of two states using a microwave pulse. Momentum is transferred to one state in this superposition by adiabatically transferring it from the $m_f=0$ sublevel to the highest- (or lowest-) lying m_f level. Adiabatic transfer is used subsequently to manipulate and ultimately to overlap the wave packets. A final microwave pulse is then used to interfere these wave packets. This method can transfer up to $2m_f\hbar k$ momentum to one arm of the interferometer. The primary limitation to the utility of this method is that the adiabatic transfer populates magnetic-field-sensitive sublevels. This makes the interferometer sensitive to Zeeman shifts. While such an interferometer may demonstrate a high sensitivity, it remains to be seen whether it can achieve high accuracy.

Finally, the ac Josephson effect in arrays of Bose-Einstein-condensed atoms [29] has recently been used to make a proof-of-principle gravity measurement. In this approach, condensate atoms tunnel from an array of vertically spaced lattice sites. Atoms tunneling from different sites subsequently interfere. The resulting interference pattern is a periodic train of atom pulses whose frequency depends on the strength of the gravitational potential. This frequency can be measured with high accuracy using conventional atom-detection techniques. A major technological drawback to this technique is the need for Bose-Einstein-condensed atomic sources, which still are difficult to produce and not suitable for a portable apparatus. Also, the time required to condense atoms is typically in excess of 30 s, which results in a low instrument bandwidth. However, if techniques to produce robust, BEC atom sources improve, this method may become viable for future instruments.

B. Direct gradient measurements

1. Multiloop interferometers

There are several Raman-pulse-based schemes that can be used for direct gravity-gradient measurements. The simplest of these is the double-loop, or figure-eight, interferometer [31]. This geometry can be achieved in the light-pulse method by inserting an extra π pulse into the light-pulse sequence. Instead of applying a $\pi/2$ pulse for the third pulse, the two atomic wave packets are allowed to pass through each other and form a second loop [see Fig. 10(b)]. Next a second π pulse redirects the wave packets to close the second loop, and a final $\pi/2$ pulse interferes the wave packets. This pulse sequence directly produces a phase shift proportional to the gravity gradient by essentially performing a coherent subtraction of two spatially, and temporally, separated gravity measurements (one for each loop). Following the pulse rules presented in Sec. I, the double-loop phase shift is given by $\Delta\phi=\phi(t_1)-2\phi(t_2)+2\phi(t_3)-\phi(t_4)$, where $\phi(t_i)$ is the phase of the ith Raman pulse at the position of the atomic wave packet at time t_i. For a given fountain height the double-loop interferometer is maximally sensitive when the interferometer spans one half of the total fountain time. Evaluating this phase, assuming a linear gravitational gradient $g(z)=g_o+\alpha z$ along the sensitive axis, gives $\Delta\phi \approx 8kg_o\alpha T^4$, where g_o is the gravitational component along the Raman wave vector at the atoms' initial position and α is the linear gradient. This formula is valid for an interferometer in the first half of a fountain of length $8T$ and for $\alpha z' \ll g_o$, where z' is the total height of the fountain.

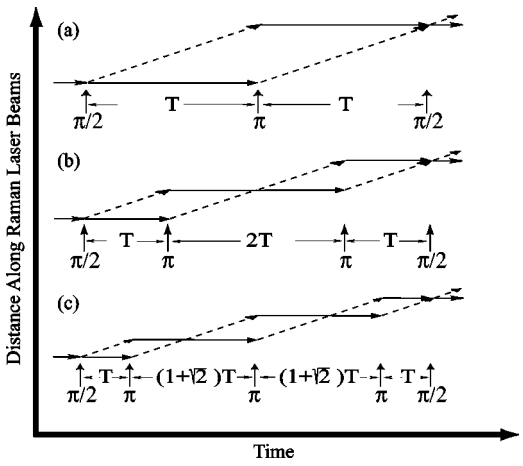

FIG. 10. Recoil diagrams for various interferometer pulse sequences. Dotted lines represent the $F=4$ states and solid lines are the $F=3$ state. The sensitivity to accelerations is proportional to the area enclosed in the recoil diagrams. The timing of π and $\pi/2$ pulses are shown with the vertical arrows. (a) Single-loop accelerometer. (b) Double-loop gradiometer. (c) Triple-loop gradiometer.

One problem with this approach is that if the interferometer spans the whole fountain time, i.e., is symmetric about the fountain's peak, then the gravity signal from each loop will be identical, resulting in no phase shift. Thus, to obtain gradient sensitivity, the double loop must be used only in the first half or the second half of the fountain, which severely constrains the possible instrument sensitivity. (This means the maximum interaction time for our fountain is $T=39$ ms, resulting in 3000 times less sensitivity to gradients as compared with two single-loop interferometers that are separated by 10 m.) In addition to this sensitivity limit, it is difficult to make the gradiometer baseline arbitrarily large and there is no common-mode vibration rejection, since each of the two acceleration measurements that comprise the grav-

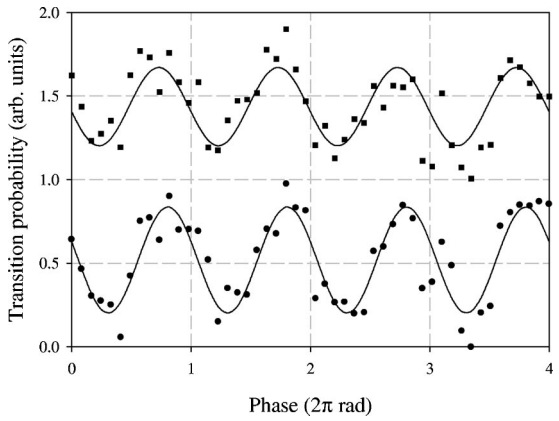

FIG. 11. Typical interference fringes from $T=44$ ms triple-loop interferometers in the upper and lower chamber. The solid lines are least-squares fits. The phase difference between the two fringes represents a measurement of the second moment of the gravitational field.

ity gradient signal are made at differing times.

A slight modification of the double-loop method allows full use of the fountain interaction time, resulting in a threefold increase in sensitivity from a double-loop interferometer in an apparatus of equivalent size. This modified sequence uses an extra π pulse in a $\pi/2$-π-π-π-$\pi/2$ sequence, which creates a triple-loop interferometer as seen in Fig. 10(c). The phase shift is $\Delta\phi=\phi(t_1)-2\phi(t_2)+2\phi(t_3)-2\phi(t_4)+\phi(t_5)$, which reduces to $\Delta\phi\approx[17/3+4\sqrt{2}]kg_o\alpha T^4$, again assuming a linear gradient and an interferometer that now spans the entire fountain time, $(8+4\sqrt{2})T$. This interferometer may be symmetrically spaced about the fountain's apex, so that the maximal interrogation time is $T=46$ ms for our fountain. Interference fringes from a triple-loop interferometer are shown in Fig. 11. The 10-m single-loop two-chamber gradiometer still is 1000 times more sensitive due to its larger baseline and longer effective interrogation time. In addition, the triple-loop gradiometer, similar to the double-loop, does not provide vibration rejection, has a limited baseline, and is only slightly less sensitive to magnetic fields.

2. Curvature measurements

Two multiple-loop gradiometers may be used in conjunction to measure the second moment of the gravity field, in a configuration similar to that used to measure the gradient with two single-loop interferometers, as illustrated in Fig. 2. In this case, the triple-loop gradient phase shifts obtained from two spatially separated atomic ensembles are subtracted to obtain the second-order curvature of the gravitational field. This device does have immunity to spurious vibrational noise because measurements are made simultaneously with respect to a common platform. Proof-of-principle data is shown in Fig. 11. Measurement of the second moment of the gravitational field allows differentiation between massive distant objects and less massive nearby objects that our gradiometer could not distinguish.

A more direct and sensitive way to characterize the second-order moment is to operate simultaneously three single-loop accelerometers spaced equidistantly along a single axis. The difference between gradients obtained by differencing the first and second accelerometer outputs from the second and third accelerometer outputs gives a second-moment measurement. This device should have the same benefits as the previous device and would be significantly more sensitive.

V. CONCLUSION

Future sensitivity enhancements are likely. Improvements in the number of atoms trapped and optically prepared in the correct state would allow for higher, atom-shot-noise limited SNRs. This might be accomplished using recently demonstrated atom trapping and cooling techniques [32,33]. Multiple pulse ($>2\hbar k$) techniques will provide straightforward access to large-area, high-sensitivity configurations.

It should be noted that the performance of a gravity gradiometer in a microgravity environment would be greatly enhanced due to the larger available interrogation time ($\Delta\phi\sim T^2$) without need for an atomic fountain, and such a high-sensitivity device would be ideal for tests of fundamental theories.

Finally, the current sensitivity makes the measurement of geophysical gradient signals possible. A portable absolute gradiometer would be useful for navigation, geodesy, terrain estimation, and oil and mineral exploration.

ACKNOWLEDGMENTS

We thank Todd Gustavson and Arnauld Landragin for constructing the trapping laser lock and Kurt Gibble for useful discussions regarding trapping and optical pumping. This work was supported by grants from the ONR, NASA, MURI, and NSF.

[1] T. Damour and A. Polyakov, Nucl. Phys. **B423**, 532 (1994).
[2] B. Venema, P. Majumder, S. Lamoreaux, B. Heckel, and E. Fortson, Phys. Rev. Lett. **68**, 135 (1992).
[3] P. Moore and B. Taylor, Rev. Mod. Phys. **72**, 351 (2000).
[4] M. J. Snadden, J. M. McGuirk, P. Bouyer, K. G. Haritos, and M. A. Kasevich, Phys. Rev. Lett. **81**, 971 (1998).
[5] *Atom Interferometry*, edited by P. Berman (Academic, New York, 1997).
[6] A. Peters, K. Y. Chung, and S. Chu, Nature (London) **400**, 849 (1999).
[7] A. Peters, K. Y. Chung, and S. Chu, Metrologia **38**, 25 (2001).
[8] M. Kasevich and S. Chu, Appl. Phys. B: Photophys. Laser Chem. **54**, 321 (1992).
[9] M. Kasevich and S. Chu, Phys. Rev. Lett. **67**, 181 (1991).
[10] C. Jekeli, Geophysics **58**, 508 (1993).
[11] See, for example, E. van Leeuwen, The Leading Edge **19**, 1296

(2000).
[12] A. J. Romaides, J. C. Battis, R. W. Sands, A. Zorn, D. O. Benson, Jr., and D. J. DiFrancesco, J. Phys. D **34**, 433 (2001).
[13] M. Moody and H. Paik, Phys. Rev. Lett. **70**, 1195 (1993).
[14] F. van Kann, M. Buckingham, C. Edwards, and R. Matthews, Physica B **194**, 61 (1994).
[15] J. Goodkind, Rev. Sci. Instrum. **70**, 4131 (1999).
[16] J. Brown, T. Niebauer, F. Klopping, and A. Herring, Geophys. Res. Lett. **27**, 33 (2000).
[17] M. H. Levitt, Prog. Nucl. Magn. Reson. Spectrosc. **18**, 61 (1986).
[18] A. Abragam, *The Principles of Nuclear Magnetism* (Oxford University Press, Oxford, England, 1961).
[19] P. Bouyer, T. L. Gustavson, K. G. Haritos, and M. A. Kasevich, Opt. Lett. **21**, 1502 (1996).
[20] J. M. McGuirk, G. T. Foster, J. B. Fixler, and M. A. Kasevich, Opt. Lett. **26**, 364 (2001).
[21] J. S. Shirley, Opt. Lett. **7**, 537 (1982).
[22] J. J. Synder, R. K. Raj, D. Bloch, and M. Ducloy, Opt. Lett. **5**, 163 (1980).
[23] J. M. Hensley, A. Peters, and S. Chu, Rev. Sci. Tech. **70**, 2735 (1999).
[24] W. M. Itano, J. C. Bollinger, J. M. Gilligan, D. J. Heinzen, F. L. Moore, M. G. Raizen, and D. J. Wineland, Phys. Rev. A **47**, 3554 (1993).
[25] Y. Tamura, Bulletin d'Informations Mares Terrestres **99**, 6813 (1987).
[26] J. M. McGuirk, M. J. Snadden, and M. A. Kasevich, Phys. Rev. Lett. **85**, 4498 (2000).
[27] D. M. Giltner, R. W. McGowan, and S. A. Lee, Phys. Rev. Lett. **75**, 2638 (1995).
[28] S. B. Cahn *et al.*, Phys. Rev. Lett. **79**, 784 (1997).
[29] B. P. Anderson and M. A. Kasevich, Science **282**, 1686 (1998).
[30] P. D. Featonby *et al.*, Phys. Rev. Lett. **81**, 495 (1998).
[31] J. Clauser, Physica B **151**, 262 (1988).
[32] S. E. Hamann, D. L. Haycock, G. Klose, P. H. Pax, I. H. Deutsch, and P. S. Jessen, Phys. Rev. A **61**, 1972 (1998).
[33] P. Treutlein, K. Y. Chung, and S. Chu, Phys. Rev. A **63**, 051401 (2001).